

BeltCrack: the First Sequential-image Conveyor Belt Crack Detection Dataset and Its Baseline with Triple-domain Feature Learning [★]

Jianghong Huang^a, Luping Ji^{a,*}, Xin Ma^b and Mao Ye^a

^aSchool of Computer Science and Engineering, University of Electronic Science and Technology of China, Chengdu, 611731, Sichuan, China

^bSuzhou Red Shield Intelligent Manufacturing Co., Ltd., Suzhou, 215000, China

ARTICLE INFO

Keywords:

Belt Crack Detection
Sequential-image Datasets
Triple-domain Feature Learning
Wavelet Frequency Transformation

ABSTRACT

Conveyor belts are important equipment in modern industry, widely applied in production and manufacturing. Their health is much critical to operational efficiency and safety. Cracks are a major threat to belt health. Currently, considering safety, how to intelligently detect belt cracks is catching an increasing attention. To implement the intelligent detection with machine learning, real crack samples are believed to be necessary. However, existing crack datasets primarily focus on pavement scenarios or synthetic data, no real-world industrial belt crack datasets at all. Cracks are a major threat to belt health. Furthermore, to validate usability and effectiveness, we propose a special baseline method with triple-domain (*i.e.*, time-space-frequency) feature hierarchical fusion learning for the two whole-new datasets. Experimental results demonstrate the availability and effectiveness of our dataset. Besides, they also show that our baseline is obviously superior to other similar detection methods. Our datasets and source codes are available at <https://github.com/UESTC-nnLab/BeltCrack>.

1. Introduction

The industrial conveyor belt is a type of raw material conveying equipment that is an indispensable core equipment in industrial production or manufacturing to realize continuous and automated material transportation [1]. Their stable operation is directly related to the operating efficiency of the production line and the safety of workers. On one hand, efficient and stable conveying can ensure smooth production processes and improve overall production capacity. On the other hand, equipment failure can cause downtime, material accumulation, and even serious accidents [2, 3]. Among various potential risks affecting belt health, belt cracks are the main hidden danger that threatens the safety of conveyor belts, mainly caused by foreign intrusion and material aging [4, 5].

From a safety perspective, the accurate detection of belt cracks has long been a major concern in the industry [6]. Currently, the primary approach is to identify cracks in an early stage, thereby preventing their further expansion and avoiding severe outcomes such as conveyor belt breakage. This practice not only safeguards production safety, but also effectively reduces economic losses by avoiding unexpected downtime and repair costs [7]. At present, how to automatically detect belt cracks is becoming a urgent issue. In this context, the vision-based machine learning method has become indispensable to ensure operational efficiency and production safety, as it enables high-speed, efficient, and noninvasive detection of structural flaws while minimizing operational disruptions [8, 9].

However, by now, learning-based belt crack detection methods have not widely explored, possibly due to the

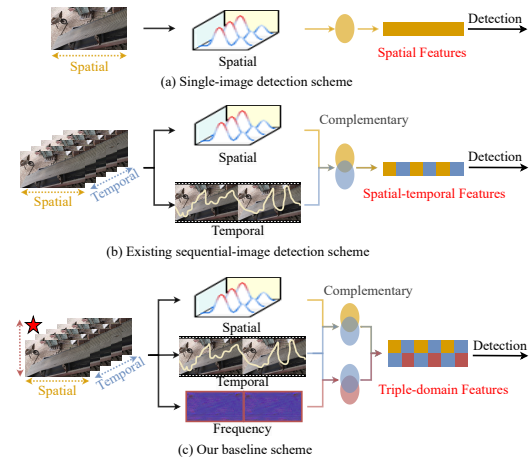


Figure 1: Comparison of three typical detection schemes for belt cracks: (a) single-image detection, (b) sequential-image detection, and (c) our triple-domain detection scheme.

serious lack of real-world datasets, besides existing several synthetic ones such as MBTID [10] and CBCD [11], even some non-belt ones such as CrackSeg5k [12]. Some possible reasons to explain this lack possibly contain two main items. One is the confidentiality requirements of production or manufacturing enterprises. The other is that the complex operational environments of industrial equipment (e.g., high radiation, high temperature or pressure) make on-conveyor-line data collection extremely difficult, hindering the acquisition of sufficient samples with diverse defect morphologies.

To fill in the dataset gap of real-world industrial conveyor belt crack detection, and propel the advancement of machine learning methodologies in this field, this paper constructs a pair of sequential-image datasets (BeltCrack14ks and BeltCrack9kd) specially for belt crack detection. Not

[★]This work is supported by the National Natural Science Foundation of China (NSFC) under Grants 62476049 and 62276048.

*Corresponding author

✉ jianghong@std.uestc.edu.cn (J. Huang); jiluping@uestc.edu.cn (L. Ji); hongdunalarm@163.com (X. Ma); cvlab.uestc@gmail.com (M. Ye)

synthetic, they both are collected by the real video cameras on the moving raw-material conveyor lines of a steel enterprise, with the laborious image-wise annotations by manual means. To the best of our knowledge, this pair of whole-new belt crack datasets are the first ones from real-world industrial scenes. By solving the lack problem of datasets, they could effectively support the learning-based method study in belt crack detection field.

Besides, in order to verify the availability and effectivity of generated datasets, we need to choose some detection methods for experiments. However, almost no learning-based method is available specially for real-world belt crack detection. Some similar methods, such as PyramidFlow [13], RIND [14] and AOST [15], are proposed only for general object detection or crack segmentation. These similar ones could usually be grouped into two primary categories. One is the single-image category of detection methods only with spatial feature learning [16]. The other is the sequential-image category of detection methods with spatial-temporal fusion feature learning. The former, only utilizing the spatial features of single image [17, 18], whose typical framework is shown in Fig. 1(a), cannot capture the temporal features from sequential-image samples. In the meanwhile, for the latter, whose typical framework is shown in Fig. 1(b), although it has extended the feature learning from spatial domain to spatial-temporal domain [19, 20], more feature domains have not been considered yet [21].

In view of these actualities, it is believed to be potential that we utilize more feature domains (*e.g.*, frequency) to promote crack detection performance [22, 23]. Therefore, we propose a baseline detection method of triple-domain feature hierarchical fusion learning with wavelet frequency, specially for our new datasets.

As shown in Fig. 1(c), surpassing classic spatial-temporal features, it can effectively capture spatial-temporal-frequency features and hierarchically fuse them, to enhance crack detection performance. The comparison experiments on our two datasets demonstrate that our baseline detection method obviously outperforms other detection approaches.

In summary, the main contributions of our work in belt crack detection field could be summarized as follows.

(I) We collect and annotate a pair of belt crack detection datasets (*i.e.*, BeltCrack14ks and BeltCrack9kd). They are the first sequential-image moving belt crack detection datasets from real-world production factory.

(II) We propose a baseline detection method for our new datasets. This baseline fully utilizes triple-domain features to enhance the detection performance on belt cracks.

(III) Extensive comparison and ablation experiments are performed to demonstrate the availability and effectivity of our whole-new datasets, as well as the superiority of our baseline method.

2. Related Work

2.1. Crack Detection Datasets

Although industrial conveyor belts are widely used in modern production systems, there remains a critical scarcity

of real-world datasets for belt crack detection, which significantly hinders the development and deployment of machine learning in this field. Existing crack datasets could be divide into non-belt crack datasets and belt crack datasets.

(1) Non-belt Crack Datasets

These non-belt crack datasets mostly originate from infrastructure scenarios like road surfaces and wall surfaces, and even include artificially synthesized data.

Crack500 [24] includes 500 crack images from pavement surfaces taken by phones. CrackMap [25] is created for a road crack segmentation study, including 114 samples. CrackSeg5k [12] is collected from nuclear power plants consisting of 2,000 original images. In addition, there are some composite datasets, which are formed by collating numerous small-scale datasets. CrackSeg9k [26] integrates 9,255 crack images from open-source datasets in diverse scenarios, including masonry walls, road surfaces, ceramic substrates, and bridge decks. OMNICRACK30K [27] establishes a cross-domain benchmark for universal crack segmentation, spanning diverse substrates including asphalt, steel. TUT [28] comprises 1,408 images across 8 scenarios (bitumen, cement, bricks, etc.), with 138 samples from the internet.

(2) Belt Crack Datasets

Compared with non-belt crack datasets, belt crack datasets feature higher collection difficulty and smaller data volume, primarily due to two factors. Firstly, data confidentiality poses a major obstacle, sharing such data could potentially expose trade secrets or competitive advantages. Secondly, conveyor belts typically operate in enclosed, high-temperature, and dusty environments, making data collection often require production shutdowns.

MBTID [10] comprises 1,708 images of belts (372 tears, 491 scratches, 845 intact images), with part of the data sourced from real industrial sites and the other part from laboratory-simulated data, where smoke generators and other methods were used to artificially simulate actual environmental conditions. CBCD [11] includes 1,562 crack samples. The images were collected from mountain tunnel construction sites, experiment setup stations and using web crawling techniques.

However, these datasets are either from non-industrial belt scenarios or synthetic. Moreover, they only include single-frame images in various states, which can't reflect the dynamic formation of cracks.

2.2. Learning-based Crack Detection

To ensure the safety and reliability of industrial infrastructure, crack detection is a critical task. However, no dedicated methods are currently available for the detection of belt cracks. Existing approaches primarily consist of two categories: single-image detection methods and sequential-image detection methods.

(1) Single-image Detection

The single-image detection method only extracts spatial features from one single frame to achieve certain detection accuracy, typically with lower computational complexity

[16, 29]. RIND [14] proposes an edge detection method for four crack types, simultaneously detecting their edges by focusing on their inter-type relationships. JTFN [30] contributes by integrating an iterative feedback learning strategy to jointly model global topological structures and refined local features, with a specific focus on capturing curvilinear crack patterns. ADL4VAD [31] introduces adaptive bias in abnormal sample data to highlight the detection results of abnormal targets.

(2) Sequential-image Detection

In contrast, sequential-image leverages spatial-temporal analysis of consecutive frames to capture crack formation trends and dynamic morphological changes. vid-TLDR [19] proposes training-free token merging for lightweight video transformer that aims to enhance the representation of video targets. TAPTR [20] propose a transformer-based arbitrary point tracking framework, treating each target point in video frames as a point query to enable target detection and tracking.

However, the aforementioned methods face inherent limitations that render them inadequate for real-world scenarios. The single-image approach struggles with high-speed motion blur, often missing minor cracks due to weakened edge features. In addition, sequential-image methods cannot handle periodic belt deformation (such as conveyor shaft extrusion) and cannot distinguish cracks from textures or stains.

3. BeltCrack Datasets

3.1. Dataset Construction

(1) Video Capturing Equipment

Due to the spatial constraints in industrial environments, we collected data using the uniform smartphones for portability, with camera resolutions in 16 : 9 ratio including 3840×2160 and 1920×1080, and an image frequency acquisition of 30 FPS. To ensure stably capture, smartphones were mounted on adjustable tripods, minimizing the motion blur during data collection.

(2) Capturing Environment

The datasets are captured in real-world industrial environments, including conveyor the belt cracks under multiple perspectives (top-down, bottom-up), varying the lighting conditions from morning strong light to evening low illumination, extreme weather (sunny, rainy, snowy), and dynamic belt moving speeds.

(3) Processing and Annotation

Original acquisition data is a three-channel video data stream, and each frame image only contains red, green and blue color space information. Based on the visual saliency and distribution density of crack features, we divided the collected data specifications into two special sub-datasets: BeltCrack14ks (strong saliency, dense crack scenes) and BeltCrack9kd (weak saliency, sparse crack scenes). Each original video is split into a sequence dataset, and finally a hierarchical data structure that conforms to the COCO specification is constructed through frame-by-frame pixel-level

Table 1

Overall statistics. Sub.: dataset subsets, Img.: image number, Seq.: sequence number, CN: crack number, $Img_{-avg/seq}$: average image number per sequence, $CN_{avg/img}$: average crack number per image, Obs.: obscured. By region size (pixels), cracks are area-categorized into: tiny (< 100), small ($100 \rightarrow 1000$), medium ($1000 \rightarrow 10000$), large ($10000 \rightarrow 100000$), and huge (≥ 100000).

Datasets	Sub.	Img.	Seq.	CN	$Img_{-avg/seq}$	$CN_{avg/img}$	Obs.	Tin.	Sma.	Med.	Lar.	Hug.
BeltCrack14ks	train	8773	18	21475	487.39	2.79	✓	5	588	12083	8755	44
	val	2596	5	7899	519.20	3.04	✓	12	573	4700	2607	7
	test	2718	6	7932	453	2.92	✓	16	1117	3596	3196	7
BeltCrack9kd	train	7697	33	10405	233.24	1.35	✓	-	16	2056	6330	2003
	test	1948	9	2482	216.44	1.27	✓	-	2	362	767	1351

bounding box annotations. Given current time constraints, our dataset currently focuses on a one-class cracks, while it inherently supports the future expansion to multi-class classification.

3.2. Datasets Statistics

We analyze the data distribution of these two datasets from many aspects, including crack spatial distribution, environmental diversity, temporal sequences.

The dataset BeltCrack14ks contains 14,087 images, across 29 sequences. It is divided into training, validation, and test sets (6:2:2 splitting), while BeltCrack9kd comprises 9,645 images, from 42 sequences with an 8:2 training and test split. Comparative analysis reveals that, BeltCrack14ks has higher average crack quantity, i.e., BeltCrack14ks 2.65 vs. BeltCrack9kd 1.34, and longer sequences (the former 485.76 vs. the latter 229.64 frames, per sequence). Their comparisons imply that BeltCrack9kd could have lower metrics, increasing the level of detection challenges. Furthermore, we quantify their crack saliency through irregular area computations, to characterize their distribution patterns, with the statistical breakdowns provided in Table 1.

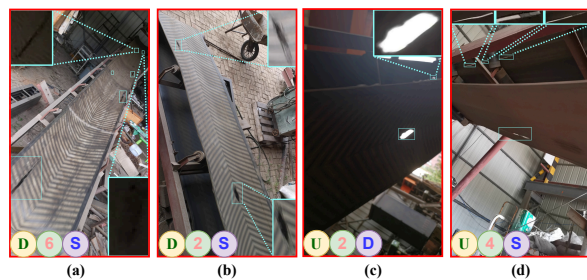


Figure 2: Samples in BeltCrack14ks with three tags: camera angle, number of cracks, lighting condition. (a) Down, 6 cracks and standard light. (b) Down, 2 cracks and standard light. (c) Up, 2 cracks and dim light. (d) Up, 4 cracks and standard light.

Moreover, the two datasets were acquired under 4 diversified conditions: multi-angle captures, time-varying illumination (e.g., morning, noon, dusk, with auxiliary lighting), multi-weather scenarios (e.g., sunny, snowy, overcast), and varying conveyor moving speeds (2-6 m/s). This group of systematic environmental variations ensures the robust data

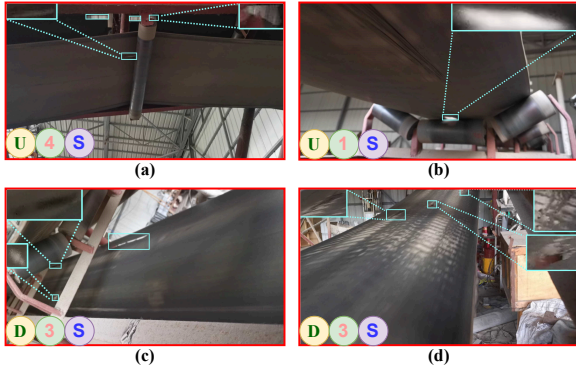


Figure 3: Samples in BeltCrack9kd with three tags: camera angle, number of cracks, lighting condition. (a) Up, 4 cracks and standard light. (b) Up, 1 cracks and standard light. (c) Down, 3 cracks and standard light. (d) Down, 3 cracks and standard light.

diversity for model generalization. As demonstrated in Fig. 2 and Fig. 3, through four representative samples from each dataset, our two belt crack datasets exhibit unprecedented environmental diversity, compared with all the other datasets in Table 2.

As quantified in Fig. 4, by (a) and (b), in spatial distribution analysis, BeltCrack9kd exhibits significantly higher crack discreteness, so there is potential to investigate sparse discrete-distributed crack features. In addition, we divide all the cracks in the datasets according to their area sizes, and their division criterion shown by the crack region size (pixel) in Table 1. As shown in Fig. 4, in (c) and (d), the both datasets exhibit the area distributions that approximate normal distributions with long-tailed characteristics. In other words, the samples in our datasets seem sufficient, diverse and statistically representative. They could help us to fully study the crack characteristics. Moreover, their sequence length distributions are shown in Fig. 4 (e) and (f). Both datasets exhibit uneven sequence lengths, primarily due to the high-speed conveyor belt moving and occlusions/limited viewing angles in industrial settings. This distribution authentically reflects real-world variability. Totally seen, BeltCrack9kd could have significant disparities, highlighting its practical relevance in industrial inspection challenges.

3.3. Superiority to Other Datasets

The proposed datasets could advance the industrial learning-based crack detection with some obvious advantages, as listed in Table 2.

(1) Larger Dataset Scale

Ours has 20K+ high-resolution industrial sequential images (continuously updated), along with high-density crack annotations.

(2) Sequence-based Datasets, not Image-based

Our datasets are the first crack benchmark library for industrial time series scenarios. They break through the

traditional static detection framework. Both datasets record the development of belt cracks across the operational cycles of conveyor systems.

(3) Real Industry Scene, not Synthetic

Our datasets are collected and generated from real industrial production environments, not simulated or synthesized (as MBTID [10] and CBCD [11] do) on small real-word samples by generation algorithms.

4. Proposed Crack Detection Baseline

4.1. Motivation

Currently, data-driven single-frame [8, 11] and some multi-frame schemes [32] have appeared, but not specially for industrial belt crack detection. Usually, they could not be suitable to our sequence-based belt crack detection datasets very well. At present, as stated before, almost no special detection method is specially proposed for industrial-scene moving belt crack detection. To address this issue, we propose a new baseline with triple-domain feature hierarchical fusion learning, named **BeltCrackDet**.

4.2. Overall Architecture

Our baseline is with three parallel feature extraction branches, and three types of features respectively from triple domains are hierarchically fused, as presented in Fig. 5. It receives a temporally sequence frames $I^T \in \mathbb{R}^{3 \times T \times H \times W}$ from a sample video as its original input.

In detail, T is the number of frames (a sequence fragment), H and W are the height and width of input images, respectively. We adopt the CSPDarknet [29] as our feature extractor that can be replaced with any other backbone network. Then, each frame in image set $I^T = \{I_1, I_2, \dots, I_t\}$ is fed into the backbone with shared weights. I_t is the keyframe and other preceding frames could form dynamic context information. This results in a multi-frame primary visual feature set $F^T = \{F_1, F_2, \dots, F_t\} \in \mathbb{R}^{T \times c \times h \times w}$, where c , h and w represent the channel, height, and width of features, respectively.

In order to utilize more feature patterns, we propose a tri-path network architecture to implement cross-domain representation learning through *Hierarchical Spatial-aware Module* (HSM), *Aggregative Temporal Module* (ATM), and *Wavelet-enhanced Frequency-aware Module* (WFM). In addition, *Residual Compensation Unit* (RCU) dynamically mitigates inter-domain representational gaps, while optimizing cross-domain feature fusion. Then, F_{fst} , the enhanced frequency-spatial-temporal features, are sent to the detection head for regressing crack bounding box coordinates and predicting class labels.

The HSM takes the multi-frame features F^T generated in preceding stage as its input, and derives motion features F_S from the spatial domain. Moreover, ATM is designed to extract and enhance the spatial-temporal consistency features F_T of moving cracks through aligned multi-frame inputs. In order to obtain more comprehensive features, we fully integrate the location and motion information of crack targets by

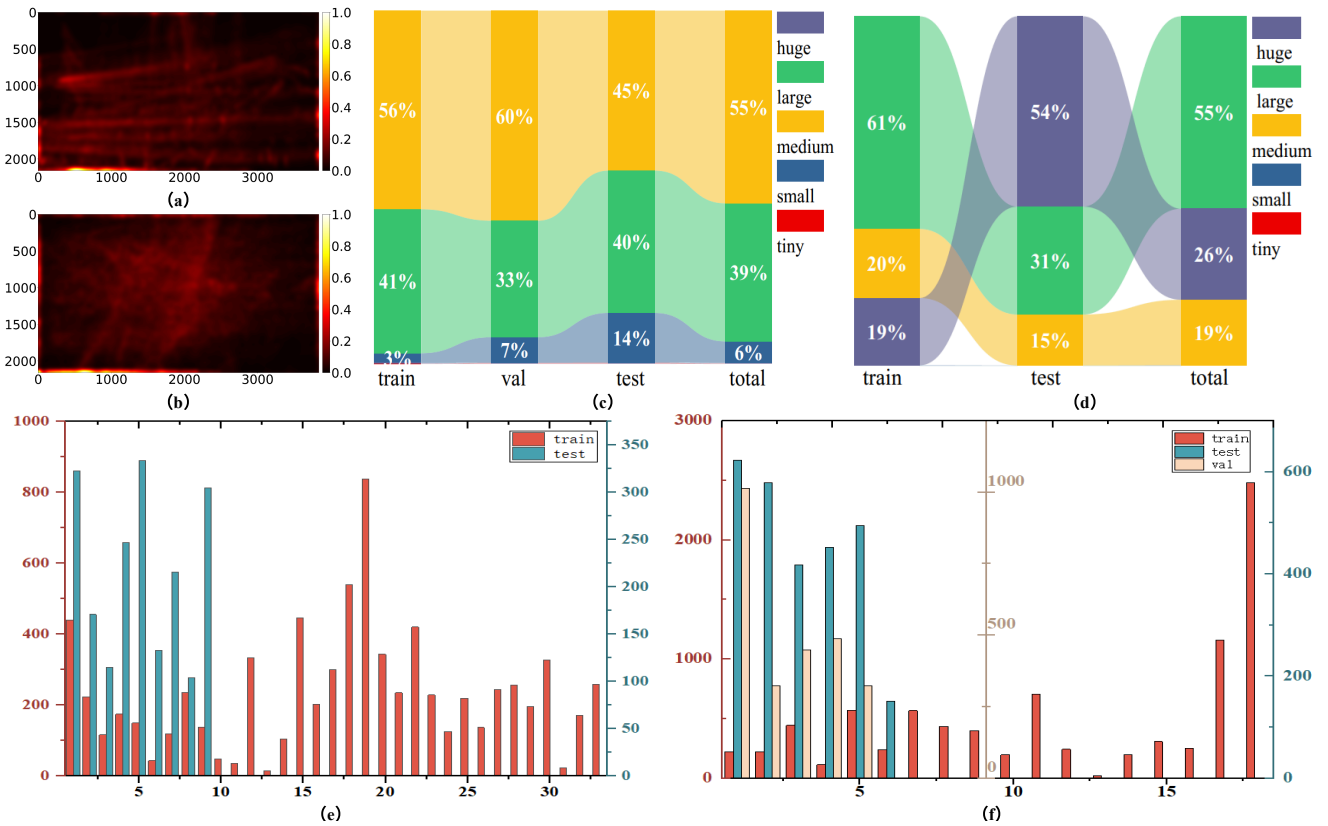


Figure 4: Sub-figures (a)-(f) visualize the crack characteristics of BeltCrack14ks and BeltCrack9kd. In detail, for each dataset, (a) and (b) indicate location distribution. (c) and (d) depict area distribution. (e) and (f) illustrate the sequence length distribution.

Table 2

Crack dataset comparisons. Types: crack types, Ind.: Industrial, Det.: detection, Seq.: sequential, Aug.: augmentation, BB: crack-level bounding box annotations, N/l: the max crack number per image, Res.: the max image resolution, Img.: total image number.

Dataset	Year	Types	Ind.	Det.	Seq.	Aug.	BB	N/l	Res.	Img.
Crack500 [24]	2019	pavement	✗	✗	✗	✓	✗	1	2000 × 1500	500
CrackSeg9k[26]	2022	collection	✗	✗	✗	✓	✗	1	400 × 400	9,255
MBTID[10]	2022	belt	✓	✗	✗	✓	✗	1	416 × 416	1,708
CBCD[11]	2023	belt	✓	✗	✗	✗	✗	1	608 × 608	1,562
CrackMap[25]	2023	road	✗	✗	✗	✓	✗	1	5184 × 3888	114
CrackSeg5k [12]	2024	wall	✓	✗	✗	✓	✗	1	7360 × 4912	2,000
OMNICRACK30K[27]	2024	collection	✗	✗	✗	✓	✗	1	4608 × 5184	30,017
TUT[28]	2025	collection	✗	✗	✗	✓	✗	1	640 × 640	1,408
BeltCrack14ks(Ours)	Current	belt	✓	✓	✓	✗	✓	10	2160 × 3840	14,087
BeltCrack9kd(Ours)	Current	belt	✓	✓	✓	✗	✓	7	2160 × 3840	9,645

concatenating spatial features F_S and temporal features F_T to obtain spatial-temporal features F_{st} , as follows:

$$F_{st} = \text{Conv}(\text{Concat}[F_S, F_T]) \quad (1)$$

where feature tensors are concatenated, and Conv has a 3×3 convolutional kernel, with BN and SiLU.

In the meanwhile, in our scheme, WFM is proposed to capture motion features in frequency domain, for better constructing the feature representations of crack objects.

$$\begin{cases} F_F = WFM(F^T) \\ F_{f_{it}} = \text{Conv}(\text{Concat}[F_F, F_T]) \\ F_{f_{gt}} = \text{Conv}(\text{Swin}(\text{Concat}[F_F, F_T])) \end{cases} \quad (2)$$

where F_F are the primary features from frequency domain. $F_{f_{it}}$ and $F_{f_{gt}}$ indicate the local and the global features fused with temporal features F_T , respectively.

Additionally, we design some RCUs to enable cross-domain feature interaction and realize the complementary

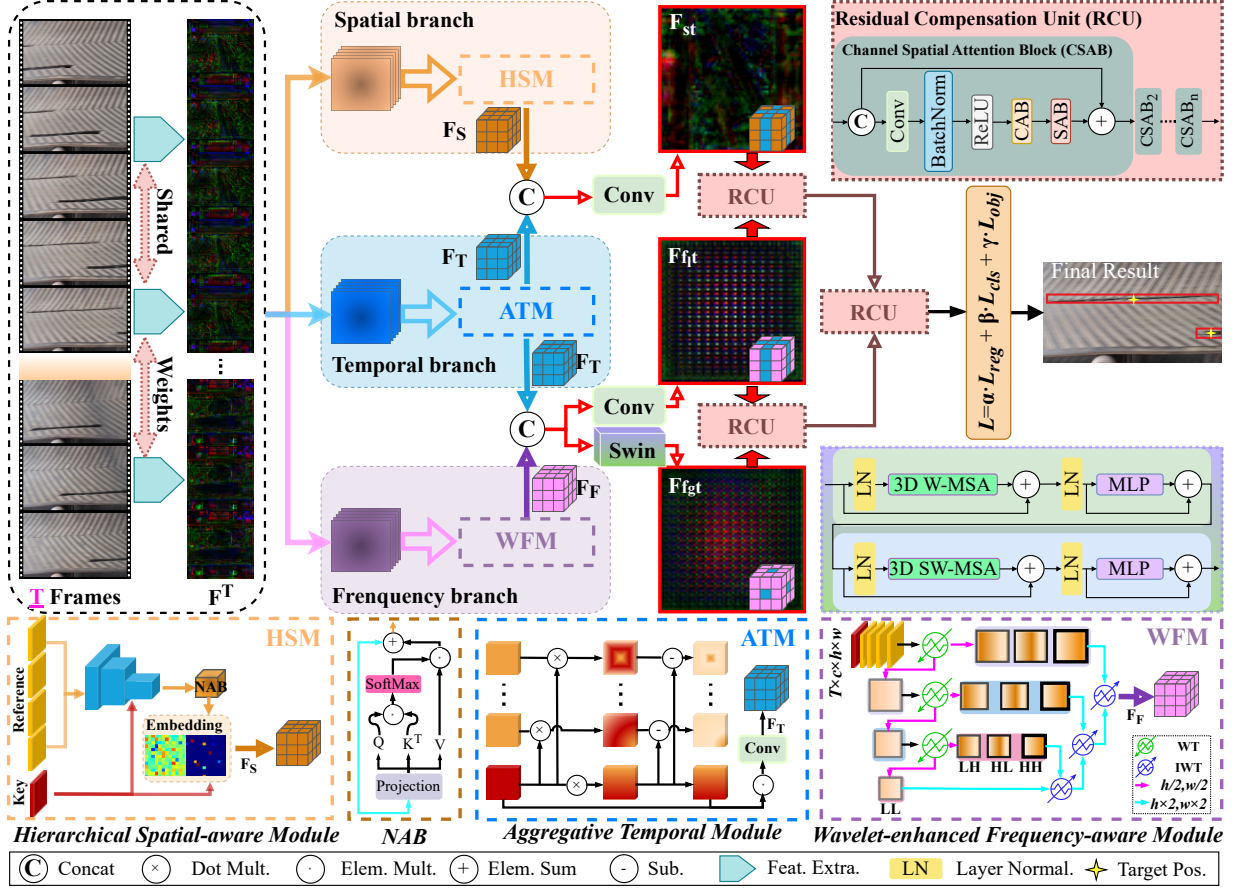


Figure 5: Overview of the proposed BeltCrackDet, including three feature branches. The first one is for spatial-domain features, the second one is for temporal-domain features, and the last is for frequency-domain features. The triple-domain features are hierarchically fused to enhance the feature representation of infrared small targets.

learning of features. The computational processes of F_{fst} , F_{ft} and F_{fst} are presented as follows:

$$\begin{cases} F_{fst} = RCU_1(F_{ft}, F_{st}) \\ F_{ft} = RCU_2(F_{fst}, F_{ft}) \\ F_{fst} = RCU_3(F_{fst}, F_{ft}) \end{cases} \quad (3)$$

where F_{fst} and F_{ft} denote the local- features and the global-level features, respectively. While F_{fst} are the compensatory frequency-spatial-temporal features obtained by RCU. Finally, the crack detection results could be obtained by the decoupled head of YOLOX [29] with non-maximal suppression.

4.3. Hierarchical Spatial-aware Module

The cross-frame spatial context information is crucial for industrial conveyor belt crack detection, as it models spatial dependencies to resolve possible ambiguities such as occlusion and motion blur. Therefore, our HSM is proposed to systematically capture these complex spatial relationships, as shown in Fig. 5. With the help of *Non-local Attention*

Block (NAB) and *Memory Enhancement Unit* (MEU), HSM could capture longer-distance feature relationships.

Specifically, inspired by the visual tracking system [21], we divide the primary feature set F^T into reference frames and keyframe. Each reference frame is assigned different weight to fuse with the keyframe, through the following process.

$$\begin{cases} \hat{F}_t &= \sigma(\text{Conv}(\text{Concat}[F_1, \dots, F_{t-1}])) \odot F_t \\ \sigma(x) &= \frac{1}{1+e^{-x}} \\ F_t &= \text{Conv}(\text{Concat}[\hat{F}_t, F_t]) \end{cases} \quad (4)$$

where \odot denotes element-wise multiplication, \hat{F}_t is an updated feature map, and F_t indicates local inter-frame spatial relations.

Furthermore, NAB is introduced to capture the long-distance dependencies between pixels in different time steps. In NAB, the feature map from F_t is sent to explore the correlation between different pixels across frames, overcoming the local limitations of convolutional layers, expressed as follows:

$$\begin{cases} (\mathbf{Q}, \mathbf{K}, \mathbf{V}) = \text{MatMul}(\mathbf{F}_l, (\mathbf{W}^Q, \mathbf{W}^K, \mathbf{W}^V)) \\ \mathbf{F}_g = \text{Softmax}\left(\frac{\mathbf{Q} \times \mathbf{K}^T}{\sqrt{d_k}}\right) \times \mathbf{V} + \mathbf{F}_l \end{cases} \quad (5)$$

where $\mathbf{W}^Q, \mathbf{W}^K, \mathbf{W}^V$ are learnable matrices, and $\sqrt{d_k}$ is a parameter for normalization. Moreover, \mathbf{F}_g represents the local-global spatial relations of neighbor frames. By NAB, any pixel pairs could interact and establish long-range dependencies, no longer confined to local neighboring pixels.

Moreover, MEU is designed to expand belt crack features. Similar to human visual tracking system, it is based on a motion storage-query mechanism. In detail, the local-global spatial features \mathbf{F}_g are stored in memory, while the keyframe features \mathbf{F}_l are used as query. Their corresponding key-value pairs are generated as follows.

$$\begin{cases} \mathbf{K}_Q, \mathbf{V}_Q &= \text{Conv}_Q^K(\mathbf{F}_l), \text{Conv}_Q^V(\mathbf{F}_l) \\ \mathbf{K}_M, \mathbf{V}_M &= \text{Conv}_M^K(\mathbf{F}_g), \text{Conv}_M^V(\mathbf{F}_g) \end{cases} \quad (6)$$

where Conv_Q and Conv_M denote different embedding layers. K serves to align the spatial location information of cracks, while V captures the high-level semantic features of these cracks.

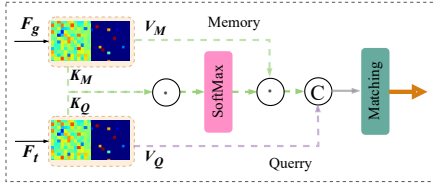


Figure 6: Overflow of MEU. It establishes the connection between keyframe and its reference frames.

As shown in Fig. 6, by constructing key-value pairs, it could comprehensively leverage multi-frame features to effectively capture the spatial interconnections among the cracks in conveyor belts.

4.4. Aggregative Temporal Module

How to extract the motion characteristics of belt cracks is a challenging problem in industrial scenarios, due to the fast motion of belts. Generally, crack features are highly susceptible to environmental factors, such as deformation and abnormal objects, making the extraction of motion features between neighboring frames challenging. Our ATM addresses this challenge by introducing a contextual aggregation mechanism, as shown in Fig. 5.

In detail, each feature in \mathbf{F}^T is fed into the ATM to fully exploit the additional motion information between consecutive frames. As shown in Eq. (7), it is employed to aggregate both inter-frame and intra-frame crack information. First, we compute the affinity weights between two frames by the dot product, where \mathbf{F}_i denotes the i -th feature of \mathbf{F}^T , and the key frame \mathbf{F}_1 refers to the last one in \mathbf{F}^T .

$$\mathbf{C}_{(i,j)} = \mathbf{F}_i \cdot \mathbf{F}_j \quad (7)$$

Then, we additionally leverage the crack feature discrepancy maps to extract specific characteristics between one frame and its adjacent frames. The pixel-wise differences between each frame and the keyframe are computed by Eq. (8), where $d(\cdot)$ is a difference function. Besides, \mathbf{D} denotes the difference map in the Euclidean space.

$$\begin{cases} \mathbf{D}_1 = \mathbf{C}_{(1,1)}; \\ \mathbf{D}_i = d(\mathbf{C}_{(1,1)}, \mathbf{C}_{(1,i)}), i \neq 1; \end{cases} \quad (8)$$

After fusion, the final feature $\hat{\mathbf{F}}$ can be defined as Eq. (9). Specially, the second term in Eq. (9) can be interpreted as a fusion of the discrepancy maps $(\mathbf{F}_i - \mathbf{F}_1)$ and the correlation maps $\mathbf{F}_i \odot \mathbf{F}_1$. The former enables the rapid spatial localization of cracks, while the latter facilitates the feature correlation of moving cracks across sequential frames, thereby mitigating the possible miss-detection caused by conveyor motion.

$$\begin{aligned} \hat{\mathbf{F}} &= \sum_{j=1}^T \mathbf{D}_j \odot \mathbf{F}_j \\ &= \mathbf{C}_{(1,1)} \odot \mathbf{F}_1 + \sum_{j=2}^T d(\mathbf{C}_{(1,j)}, \mathbf{C}_{(1,1)}) \odot \mathbf{F}_j \\ &= \mathbf{C}_{(1,1)} \odot \mathbf{F}_1 + \sum_{j=2}^T (\mathbf{F}_j - \mathbf{F}_1) \cdot \mathbf{F}_1 \odot \mathbf{F}_j \end{aligned} \quad (9)$$

where \odot denotes the element-wise multiplication between the input feature \mathbf{F}_j and the difference map \mathbf{D}_j .

Finally, we utilize the self-attention mechanism in the Hourglass network to model long-range pixel dependencies for the feature aggregation of global contextual information.

4.5. Wavelet-enhanced Frequency-aware Module

Inspired by wavelet theory [33, 34], we propose this WFM to address the challenges of crack detection in moving belts. In wavelet domain, feature map will be decomposed to different frequency sub-bands. The high-frequency sub-bands could capture the intensity changes caused by the crack edges, while the low-frequency sub-band could represent the smooth background information [35]. Generally, frequency-domain analysis could help to suppress the conveyor belt noise from texture or stains while highlighting genuine crack features.

As shown in Fig. 5, the WFM processes each feature in \mathbf{F}^T through multi-level decomposition. In detail, the cascade wavelet decomposition is obtained by recursively decomposing the low-frequency components, and each level of the decomposition is shown in Eq. (10).

$$\mathbf{X}_{LL}^{(j)}, \mathbf{X}_{LH}^{(j)}, \mathbf{X}_{HL}^{(j)}, \mathbf{X}_{HH}^{(j)} = \text{WT}(\mathbf{X}_{LL}^{(j-1)}) \quad (10)$$

where $\mathbf{X}_{LL}^{(0)}$ represents the input feature, j is the current level, and $\mathbf{X}_{LL}^{(j)}$ indicates the low-frequency component in $\mathbf{X}_{LL}^{(j-1)}$. Additionally, $\mathbf{X}_{LH}^{(j)}$, $\mathbf{X}_{HL}^{(j)}$, $\mathbf{X}_{HH}^{(j)}$ are the horizontal, vertical, and diagonal high-frequency components of $\mathbf{X}_{LL}^{(j-1)}$, respectively.

Then, a small-kernel depth-wise convolution is performed on these different frequency maps before applying the *Inverse Wavelet Transform* (IWT) to construct the output features, as expressed in Eq. (11).

$$\mathbf{Y} = IWT(Conv(\mathbf{W}, WT(\mathbf{X}))) \quad (11)$$

where \mathbf{X} denotes the input, and \mathbf{W} represents the weight tensor of a $k \times k$ depth-wise kernel. In detail, in the four sub-bands, each will be processed by a tensor \mathbf{W} .

Moreover, on level j , the expression, Eq. (11), will be further computed by Eq. (12), where $\mathbf{W}^{(j)}$ denotes the weight kernel at current level j , and $\mathbf{X}_H^{(j)}$ represents the three high-frequency maps at level j , as described in Eq. (10).

$$\mathbf{Y}_{LL}^{(j)}, \mathbf{Y}_{LH}^{(j)}, \mathbf{Y}_{HL}^{(j)}, \mathbf{Y}_{HH}^{(j)} = Conv\left(\mathbf{W}^{(j)}, \left(\mathbf{X}_{LL}^{(j)}, \mathbf{X}_H^{(j)}\right)\right) \quad (12)$$

Through cascade decomposition, we use the following formula, Eq. (13), to fuse the features of different frequencies.

$$\mathbf{Z}^{(j)} = IWT\left(\mathbf{Y}_{LL}^{(j)} + \mathbf{Z}^{(j+1)}, \mathbf{Y}_H^{(j)}\right) \quad (13)$$

Specifically, on level j , we use the expression Eq. (14) to reconstruct the high-level frequency features, as follows:

$$\begin{cases} \mathbf{Y}_n^{(j)} = \mathbf{Y}_{LL}^{(j)} + \mathbf{Z}^{(j+1)} \\ \mathbf{Z}^{(j)} = IWT(\mathbf{Y}_n^{(j)}, \mathbf{Y}_{LH}^{(j)}, \mathbf{Y}_{HL}^{(j)}, \mathbf{Y}_{HH}^{(j)}) \end{cases} \quad (14)$$

where $\mathbf{Z}^{(l+1)} = 0$, j is the number of decomposition, and $\mathbf{Z}^{(j)}$ indicates the aggregated outputs from the level j from bottom to top.

Finally, the reconstructed features $\mathbf{Z}^{(0)}$ from all levels are merged, forming a hybrid representation that preserves both spatial context and frequency-domain discriminability. By consecutively executing the process above for T times, we obtain the desired frequency-domain feature \mathbf{F}_F .

4.6. Residual Compensation Unit

Our new learning scheme thoroughly explores the spatial, temporal, and frequency domain features of belt cracks. In learning, feature mismatches could frequently occur due to the differences in the learning paths of features from these three domains. To address this problem, we design the RCU to dynamically reconcile and enhance the complementary characteristics across all three domains, aiming to effectively mitigate feature mismatch.

As shown in Fig. 5, RCU comprises several *Channel Spatial Attention Blocks* (CSAB), as presented in Eq.

(3). Specifically, local temporal-frequency features $\mathbf{F}_{f_{lt}}$ and spatial-temporal features \mathbf{F}_{st} are fused by Eq. (15). First, we channel-wise concatenate them, process them via a convolution layer with both BN and ReLU, and then refine the fused features by a dual-attention (including CAB and SAB) scheme to adaptively highlight salient regions. Finally, a residual compensation branch is added to retain critical details.

$$\begin{cases} \hat{\mathbf{F}}_e = Concat\left(\left[\mathbf{F}_{f_{lt}}, \mathbf{F}_{st}\right]\right) \\ CSAB(\mathbf{X}) = SAB(CAB(Conv(\mathbf{X}))) + \mathbf{X} \\ \mathbf{F}_{f_{lst}} = CSAB_n\left(CSAB_{n-1}\dots\left(CSAB_1\left(\hat{\mathbf{F}}_e\right)\right)\right) \end{cases} \quad (15)$$

where n is the number of CSAB. Similarly, \mathbf{F}_{ft} is obtained by the same operations on $\mathbf{F}_{f_{lt}}$ and $\mathbf{F}_{f_{st}}$. The final features of cracks, \mathbf{F}_{fst} , are also obtained from $\mathbf{F}_{f_{lst}}$ and \mathbf{F}_{ft} . In addition, $\mathbf{F}_{f_{lt}}$ is fused by a simple convolution operation with local frequency features \mathbf{F}_F and temporal features \mathbf{F}_T . Besides, $\mathbf{F}_{f_{st}}$ is fused by a *Swin Transformer* (Swin) block to capture the global information of cracks from the temporal-frequency domain.

4.7. Loss Function

In order to address the inherent challenges of severe class imbalance and extreme size variations in our datasets, we adopt a similar loss function [29] with an optimization of \mathcal{L}_{reg} . It is presented as follows:

$$\mathcal{L} = \lambda_{reg}\mathcal{L}_{reg} + \lambda_{cls}\mathcal{L}_{cls} + \lambda_{obj}\mathcal{L}_{obj} \quad (16)$$

where \mathcal{L}_{reg} , \mathcal{L}_{cls} , and \mathcal{L}_{obj} represent bounding box regression loss, classification loss, and object probability loss, respectively. \mathcal{L}_{reg} , \mathcal{L}_{cls} , and \mathcal{L}_{obj} are three hyper-parameters to balance loss terms.

For \mathcal{L}_{obj} and \mathcal{L}_{cls} , we use sigmoid focal loss [36] to solve the class imbalance of positive and negative samples in our task. In detail, the loss function in Eq. (16) can be further computed by Eq. (17):

$$\begin{cases} \mathcal{L}_{reg} = \zeta\mathcal{L}_{iou} + \eta\mathcal{L}_{nwd} \\ \mathcal{L}_{iou} = 1 - IoU(B_p, B_g) \\ \mathcal{L}_{nwd} = 1 - NWD(N_p, N_g) \\ NWD(N_p, N_g) = exp\left(-\frac{\sqrt{W_2^2(N_p, N_g)}}{C}\right) \end{cases} \quad (17)$$

where the *Normalized Wasserstein Distance* (NWD) loss is adopted in \mathcal{L}_{reg} to capture the distribution characteristics of belt cracks. C is a constant related to datasets. Besides, B_p , B_g represent the predicted box, the ground-truth box in learning, respectively. In the meanwhile, N_p and N_g indicate the Gaussian distribution of predicted boxes and the ground-truth boxes, respectively.

5. Experiments

5.1. Datasets and Evaluation Metrics

To rigorously validate the effectiveness of our new datasets, and the superiority of the proposed baseline, the comprehensive experiments on both BeltCrack14ks and BeltCrack9kd are conducted with multi-metric evaluations and performance comparisons.

Furthermore, to quantitatively assess the belt crack detection performance under industrial settings, we adopt those widely-applied metrics in general object detection frameworks, including Precision, Recall, F1, and *mean Average Precision* (mAP₅₀).

5.2. Implementation Details

Specifically, the sliding window size of sequence T is set to 5. All methods use a fixed input image size: 512×512 , to ensure fairness. Our baseline, BeltCrackDet, is trained for 100 epochs with a batch size 4. The parameter optimization in learning employs the *Stochastic Gradient Descent* (SGD) with an initial learning rate 0.01, momentum 0.937, and a cosine annealing learning rate scheduler to dynamically adjust the training stability and convergence efficiency.

The balancing hyper-parameters λ_{reg} for the regression, λ_{cls} the regression, and λ_{obj} for the object loss in Eq. (17), are experientially set to 5, 1, and 1, respectively. Besides, ζ, η are both set to 0.5. We also apply the *Non-Maximum Suppression* with a fixed *Intersection-over-Union* threshold of 0.65 in inference. Additionally, the threshold of object confidence scores is set to 0.001. Our baseline BeltCrackDet is implemented on Pytorch platform and runs on two Nvidia GeForce 4090 GPUs.

5.3. Comparisons With Other Methods

To validate the datasets and our baseline method, we choose 12 available detection methods for comparisons. These methods are grouped into two categories: single-image ones and sequential ones, as listed in Table 3.

(1) Quantitative Comparisons

Our quantitative comparison results on 13 detection methods (including ours) are displayed in Table 3. In this table, it could be easy to observe three obvious experiment findings.

The first finding is that our new datasets are *usable and practically effective* for belt crack detection. In detail, all these selected detection models can be well trained and tested on our datasets, without encountering data compatibility issues. In addition, on both datasets, the experimental results in Table 3 are discriminative enough to effectively evaluate the performance differences of different models. It implies that our datasets could make better detection methods to obtain better performance. For example, on BeltCrack14ks, JTFN [30] achieves an mAP₅₀ 40.15% and an F1 64.02%, while our baseline BeltCrackDet obtains the highest mAP₅₀ 67.08% and F1 82.17%. Similarly, JTFN [30] performs relatively poorly with an mAP₅₀ 0.66% and an F1 2.65%.

The second finding is that our new belt crack datasets (*i.e.*, BeltCrack14ks and BeltCrack9kd) seem difficult for all detection methods, the latter even more difficult than the former. In general, for an easy object detection dataset, its *state-of-the-art* (SOTA) metrics could often reach up to 98%. However, on our BeltCrack14ks, the SOTA metrics obtained by all methods are only with an mAP₅₀ 67.08%, Precision 91.03%, Recall 74.89% and F1 82.17%. In the meanwhile, on BeltCrack9kd, the SOTA metrics, *i.e.*, the mAP₅₀ 26.98%, Precision 51.06%, Recall 54.76% and F1 52.83% by BeltCrackDet, are even significantly less than those on BeltCrack14ks.

One possible reason to explain the latter more difficult than the former is that, the latter has a shorter average sequence length (*i.e.*, the $\text{Img}\cdot\text{avg}/\text{seq}$ in Table 1). This length could hinder the full learning of belt crack features. Moreover, the faster moving speed of conveyor belts in the latter also makes it more difficult.

The third one is that our baseline method could usually achieve the SOTA performance of belt crack detection on both datasets. On BeltCrack14ks, our method achieves an mAP₅₀ 67.08%, almost 1.86% higher than the second-best 65.22% obtained by AOST [15]. Besides, the Precision of BeltCrackDet could reach up to 91.03%, also obviously higher than that by the second-best one 89.71%. Furthermore, on the more difficult dataset BeltCrack9kd, although almost all methods perform poorly, with low performance metrics, our BeltCrackDet still achieves an mAP₅₀ 26.98% and Precision 51.06%, obviously superior to the second-best method AOST [15]. Meanwhile, our baseline method also has the highest metrics Recall (54.76%) and F1 (52.83%) in all 13 compared methods.

The last finding is that, the sequential-based methods are often superior to single-image detection ones. For example, on BeltCrack9kd, the SOTA mAP₅₀ by single-image method is only 24.87%, and even JTFN [30] is almost unavailable. While on same BeltCrack9kd, the SOTA mAP₅₀ could reach to 26.98% by the sequential-based BeltCrackDet (ours), with 2.11% superiority.

(2) Visualization Comparisons

To visually compare the detection capabilities of different methods on two datasets, two groups of experimental visualizations are conducted, as shown in Fig. 7. In visualization, two obvious phenomena could be observed.

Firstly, these two datasets can be used to detect belt cracks, further proving their effectiveness. For example, all selected methods can detect belt cracks in the sample, but the detection results by different methods are different. Some methods, such as our BeltCrackDet, AOST and TAPTR, can detect all cracks in the sample from BeltCrack14ks, while someone, *e.g.*, CrackFormer and JTFN, could miss belt cracks. This allows us to easily distinguish which method is better for belt crack detection.

Secondly, it is often hard to detect all belt cracks in samples, especially on more difficult BeltCrack9kd. For example, in the sample from BeltCrack14ks, some methods, including TAPTR, AOST, our BeltCrackDet, can almost

Table 3

Quantitative comparisons on both BeltCrack14ks and BeltCrack9kd. The top-three results are highlighted by underlined bold, **bold** and underlined, respectively.

Category	Methods	Publica.	on BeltCrack14ks				on BeltCrack9kd			
			mAP ₅₀	Precision	Recall	F1	mAP ₅₀	Precision	Recall	F1
Single-image	RIND[14]	ICCV'21	52.25	83.57	63.72	72.36	24.34	48.62	44.48	46.91
	YOLOX[29]	arXiv'21	61.79	81.01	<u>74.65</u>	79.29	24.82	<u>50.54</u>	49.36	50.22
	CrackFormer[16]	ICCV'21	48.71	75.57	65.56	70.21	4.17	12.76	33.88	18.54
	JTFN[30]	ICCV'21	40.15	65.23	61.79	64.02	0.66	1.38	32.03	2.65
	PyramidFlow[13]	CVPR'23	60.85	81.63	75.66	78.85	23.86	49.67	<u>53.72</u>	52.81
	CrackNex[37]	ICRA'24	62.59	82.51	74.47	79.82	24.79	50.23	52.95	50.75
	SimCrack[38]	WACV'24	<u>64.33</u>	<u>87.39</u>	73.28	<u>80.84</u>	24.87	50.79	52.18	48.67
	ADL4VAD[31]	WACV'25	52.04	79.51	61.69	71.84	21.76	47.86	47.06	45.37
	UniAS[39]	WACV'25	51.63	81.47	57.58	70.56	21.36	48.07	40.25	52.35
Sequential	vid-TLDR[19]	CVPR'24	59.11	80.89	67.72	75.94	22.42	49.35	48.12	48.18
	TAPTR[20]	ECCV'24	63.38	84.52	74.11	79.09	<u>25.06</u>	48.35	53.14	51.31
	AOST [15]	TPAMI'24	65.22	89.71	73.96	81.45	26.33	47.17	54.38	<u>52.54</u>
	BeltCrackDet (ours)	—————	67.08	91.03	74.89	82.17	26.98	51.06	54.76	52.83

detect all cracks, while other methods, *e.g.*, YOLOX, will miss true crack (*i.e.*, miss detection). Specially, on more difficult BeltCrack9kd, almost no method can correctly detect all cracks in the chosen sample with very subtle crack features. One possible reason is that, the distant cracks with heavy occlusion and weak lighting could heavily degrade the feature learning ability of detection methods.

(3) Precision-Recall Curves

To evaluate the comprehensive detection performance of our baseline method, we design two groups of experiments to generate the *Precision-Recall* (PR) curves of detection methods on both datasets. These PR curves are depicted in Fig. 8. Through comparison and analysis, two apparent findings are easily found.

One is that, on both datasets, all compared detection methods can be successfully trained and tested, merely with diverse detection performance. From the two graphs, it can be observed that the *Area Under the Curve* (AUC) for each method differs. Moreover, the AUC of the same method on BeltCrack9kd is significantly smaller than that on BeltCrack14ks. Considering the smaller AUC, the poorer comprehensive performance, this also implies that the latter is more difficult than the former.

The other is that, our baseline method almost outperforms all the others on both datasets. Notably, its PR curve consistently resides in the top-right quadrant, leading to the largest AUC (corresponding to the best comprehensive performance). This further validates the superiority of our baseline approach in belt cracks detection.

(4) Complexity Comparisons

Besides detection performance, we additionally compare the model complexity of our BeltCrackDet with 12 other representative methods. Considering the complexity is irrelative to dataset, only easy BeltCrack14k is chosen for experiments. Their quantitative comparison results are listed in Table 4, mainly including FLOPs, Params and FPS. Similarly, in this table, we could still get two discoveries.

One is that, although our method (*i.e.*, BeltCrackDet) is sequential-based one, compared to others, its FLOPs and

Table 4

Complexity comparisons of different methods on BeltCrack14ks. The best result is marked in **bold**.

Methods	Frames	mAP ₅₀ ↑	F1 ↑	FLOPs ↓	Params ↓	FPS ↑
RIND[14]	single	52.25	72.36	265.15G	8.37M	7.6
YOLOX[29]	single	61.79	79.29	29.68G	9.2M	50.8
CrackFormer[16]	single	48.71	70.21	50.58G	8.42M	17.3
JTFN[30]	single	40.15	64.02	656.48G	17.87M	1.8
PyramidFlow[13]	single	60.85	78.85	76.28G	10.27M	14.5
CrackNex[37]	single	62.59	79.82	47.35G	14.21M	13.6
SimCrack[38]	single	64.33	80.84	76.19G	9.54M	15.1
ADL4VAD[31]	single	52.04	71.84	120.72G	15.88M	11.7
UniAS[39]	single	51.63	70.56	127.02G	11.95M	12.9
vid-TLDR[19]	multiple	59.11	75.94	351.14G	46.71M	2.6
TAPTR[20]	multiple	63.38	79.09	57.28G	27.40M	13.3
AOST[15]	multiple	65.22	81.45	182.45G	33.84M	9.5
BeltCrackDet (ours)	multiple	67.08	82.17	254.04G	24.41M	9.2

Params seem moderate. In detail, it has a FLOPs of 254.04G, and a Params of 24.41M. Comparatively, JTFN [30] has an obviously-larger FLOPs (656.48G), while YOLOX [29] only has a smaller FLOPs 29.68G. Similarly, our method has a Params of 24.41M, while the Params of vid-TLDR [19] reaches up to 46.71M, and that of RIND [14] is the smallest (only 8.37M). One probable reason is that, the feature capturing and fusing module specially for frequency domain is added in our detection framework. It has to enhance the crack feature extraction across sequential-images. Nevertheless, it causes almost no excessive increase in complexity.

The other is that, with the increase of computational cost, the FPS by our BeltCrackDet will decrease to only 9.2, smaller than those by most other detection methods. For example, YOLOX [29] has a low complexity (FLOPs 29.68G and Params 9.2M) and a high FPS (50.8), however its mAP₅₀ and F1 are only 61.79% and 79.29%, respectively. On a same dataset, our baseline method is far superior to classic YOLOX. For our baseline, it is worthwhile to give up high FPS while pursuing high detection performance.

(5) Crack Heatmap Comparisons

In object detection, object heatmaps are often used for the interpretability of detection models, because they could highlight object areas by mapping object confidences into different colors. To further demonstrate the interpretability

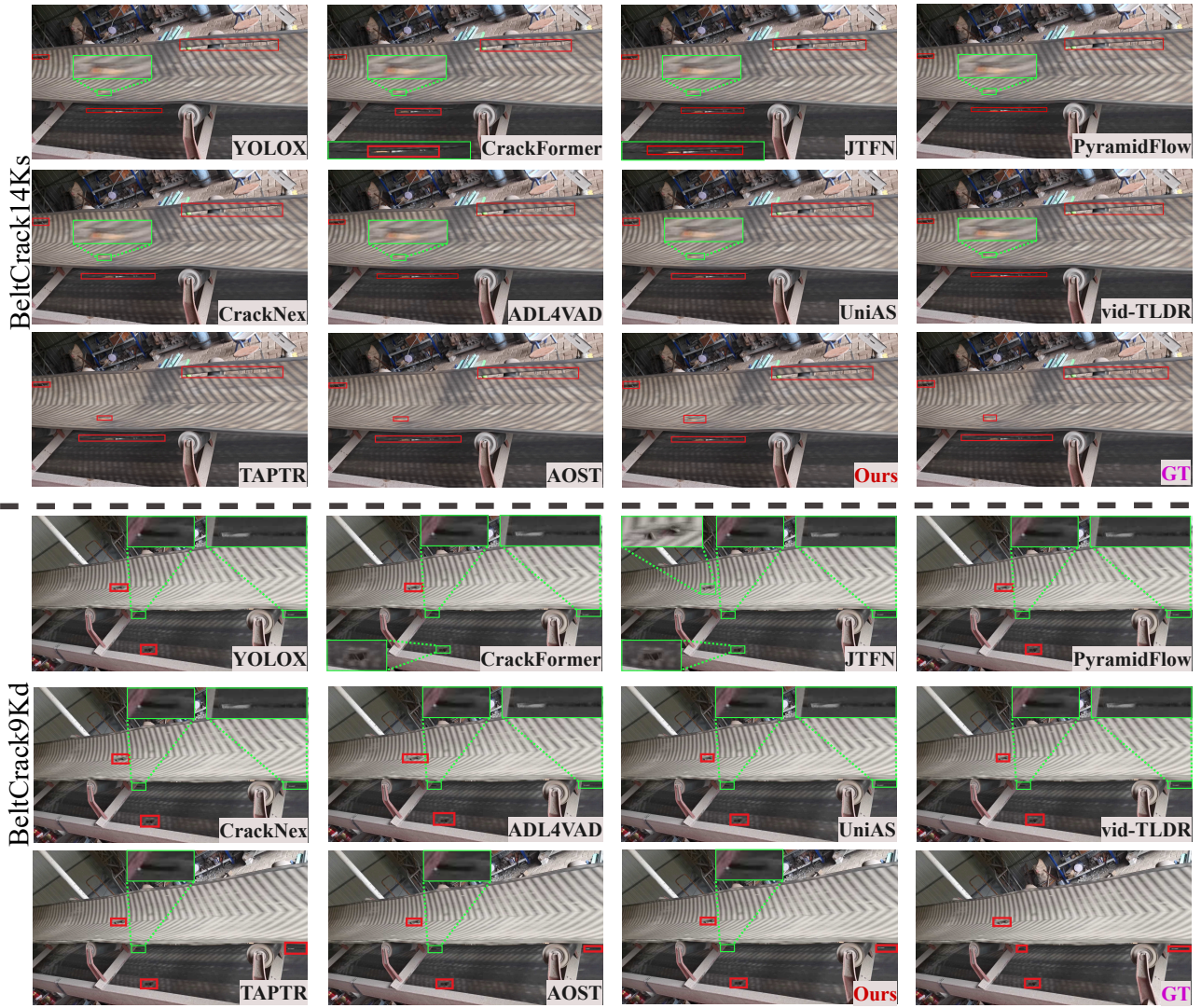


Figure 7: Visual comparison on our datasets. GT=Ground Truth. Red boxes represent detected cracks (correct), green ones indicate missed-cracks, and the green box that contains a red one indicates an incomplete crack detection.

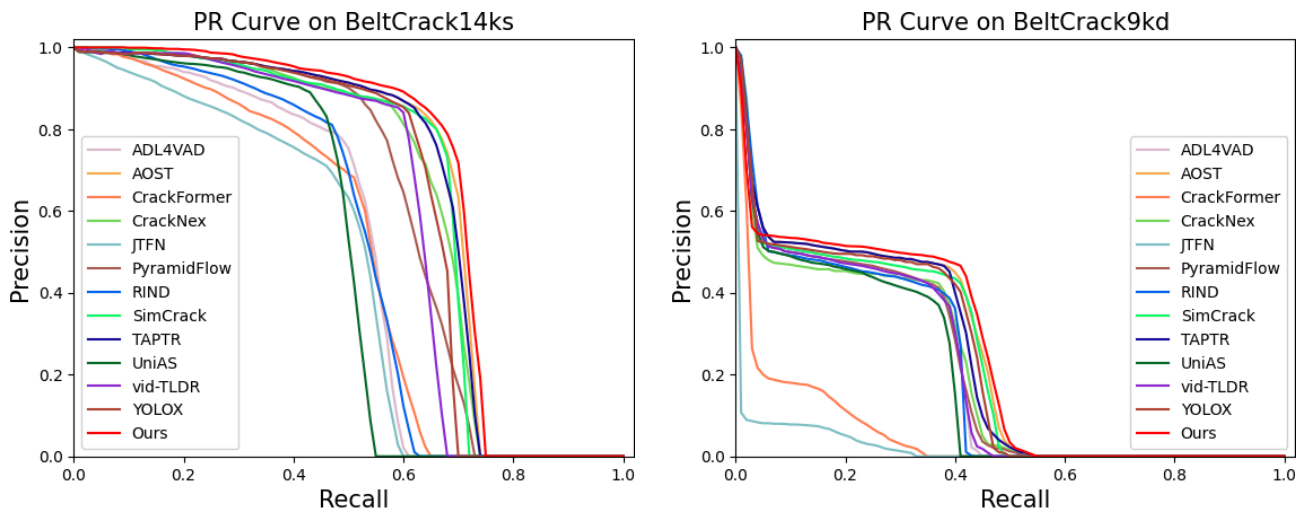


Figure 8: PR curves of 12 representative detection methods on datasets BeltCrack14ks and BeltCrack9kd.

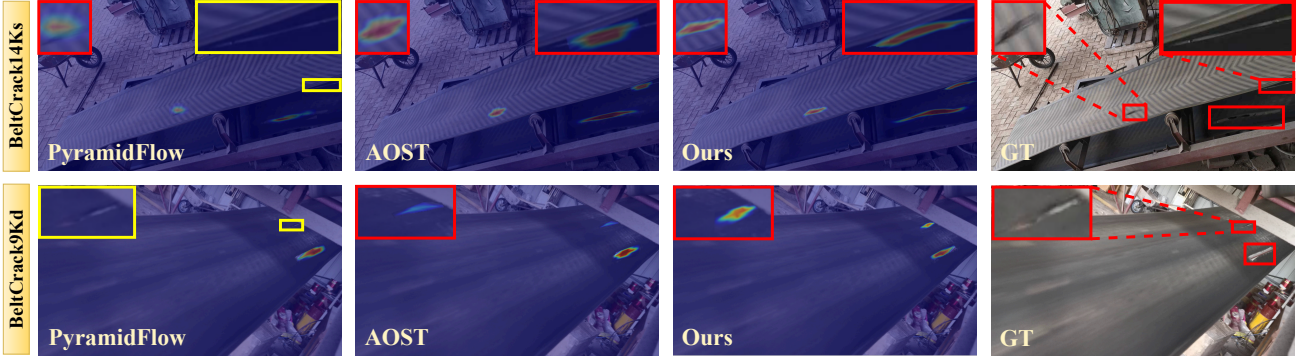


Figure 9: Heatmap visualization comparisons. Yellow boxes indicate the missed cracks, and red boxes denote the crack heatmaps and their zoomed presentations.

of our baseline method, two groups of belt crack heatmaps generated by three detection methods are computed, and then visually presented in Fig. 9, one sample for one dataset. In these belt crack heatmaps, the higher confidence is shown by the warmer color (orange), while the lower one is shown by the cooler color (blue).

By comparisons, we could easily find that the heatmaps generated by our baseline BeltCrackDet are obviously superior to those by other two representative methods, in terms of crack location, shape and miss detection. For example, on BeltCrack14ks, PyramidFlow [13] misses a tiny one (*i.e.*, miss detection) of three true cracks. In contrast, our baseline could correctly generate the heatmap for this crack. Moreover, even on difficult BeltCrack9kd, our baseline could still generate a higher-quality heatmap than PyramidFlow [13] and AOST [15]. In detail, our heatmap seems more consistent (including location and shape) to the real crack in original sample than the other two. These comparisons further verify the superiority of our baseline, as shown in Table 3.

5.4. Ablation Study

To demonstrate the characteristics of our new baseline detection method, we design three groups of ablation study, including module assembling, regression loss definition, and hyper-parameter setting.

(1) Module Effects

On both datasets, for our BeltCrackDet, we conduct a group of ablation studies to investigate the effects of different module assembling schemes on crack detection performance. They are quantitatively shown in Table 5. By comparison, we could capture two ablation findings.

One is that each module is effective in improving the detection performance to some extent. For example, on BeltCrack14ks, the baseline without any module (*i.e.*, w/o All) only achieves an mAP₅₀ of 61.01% and an F1 of 78.26%. Once HSM is applied, mAP₅₀ could rise to 63.73%, and F1 could rise to 80.01%. With ATM, mAP₅₀ and F1 could be further improved to 64.02% and 80.24%, respectively. What’s more, utilizing the frequency-domain branch without

Table 5

The ablation study on different module assembling. Specifically, R(A) only applies RCU₁, R(B) contains both RCU₁ and RCU₂, and R(C) employs all RCU components. The best metrics are marked in **bold**.

Settings	HSM	ATM	WFM	R(A)	R(B)	R(C)	on BeltCrack14ks			on BeltCrack9kd				
							mAP ₅₀	Precision	Recall	F1	mAP ₅₀	Precision	Recall	F1
w/o All	-	-	-	-	-	-	61.01	87.53	70.76	78.26	20.95	46.35	41.73	44.18
w HSM	✓	-	-	-	-	-	63.73	88.14	73.27	80.01	20.48	46.97	43.55	45.29
w HSM & ATM	✓	✓	-	-	-	-	64.02	89.65	72.62	80.24	22.19	45.73	49.19	47.42
w/o R	✓	✓	✓	-	-	-	65.16	89.89	73.92	81.13	23.36	47.18	50.08	48.59
w R(A)	✓	✓	✓	✓	-	-	66.37	90.09	74.22	79.72	24.58	48.62	51.77	50.14
w R(B)	✓	✓	✓	✓	✓	-	66.76	90.31	75.13	80.12	25.78	49.95	53.13	51.57
w R(C)	✓	✓	✓	✓	✓	✓	67.08	91.03	74.89	82.17	26.98	51.06	54.76	52.83

Table 6

Three loss function comparisons. The best metrics are marked in **bold**.

Settings	on BeltCrack14ks				on BeltCrack9kd			
	mAP ₅₀	Precision	Recall	F1	mAP ₅₀	Precision	Recall	F1
\mathcal{L}_{nwd}	65.77	87.42	78.26	80.14	23.72	47.65	53.41	50.08
\mathcal{L}_{iou}	66.39	92.11	72.19	80.35	24.49	50.68	53.15	50.73
\mathcal{L}_{reg} (with \mathcal{L}_{nwd} and \mathcal{L}_{iou})	67.08	91.03	74.89	82.17	26.98	51.06	54.76	52.83

RCU could also yield an obvious improvement, with mAP₅₀ and F1 increasing to 65.16% and 81.13%, respectively.

The other is that, the best detection performance is always acquired when all neural-network modules are applied. For example, on BeltCrack14ks, only the assembling scheme “w R(C)” could obtain the best mAP₅₀ (67.08%) and F1 (82.17%). On BeltCrack9kd, mAP₅₀ and F1 are also respectively updated to 26.98% and 52.83%.

(2) Regression Loss Effects

To validate the impacts of optimized \mathcal{L}_{reg} , we further design a group experiment with three different loss functions, as shown in Table 6. In this table, “ \mathcal{L}_{nwd} ” indicates that the loss term \mathcal{L}_{reg} in Eq. (17) is set to “ \mathcal{L}_{nwd} ” without \mathcal{L}_{iou} . “ \mathcal{L}_{iou} ” represents that \mathcal{L}_{reg} only uses \mathcal{L}_{iou} . Moreover, “ \mathcal{L}_{reg} ” denotes that the regression loss combines \mathcal{L}_{iou} and \mathcal{L}_{nwd} to balance detection accuracy and geometric consistency.

From Table 6, two obvious observations could also be obtained. One is that the \mathcal{L}_{reg} could often help our BeltCrackDet to achieve the best comprehensive performance. For example, the \mathcal{L}_{reg} gains the peak mAP₅₀ 67.08% and F1 82.17% on BeltCrack14ks. Moreover, it also achieves the highest evaluation metrics (including mAP₅₀, Precision, Recall and F1) on dataset BeltCrack9kd.

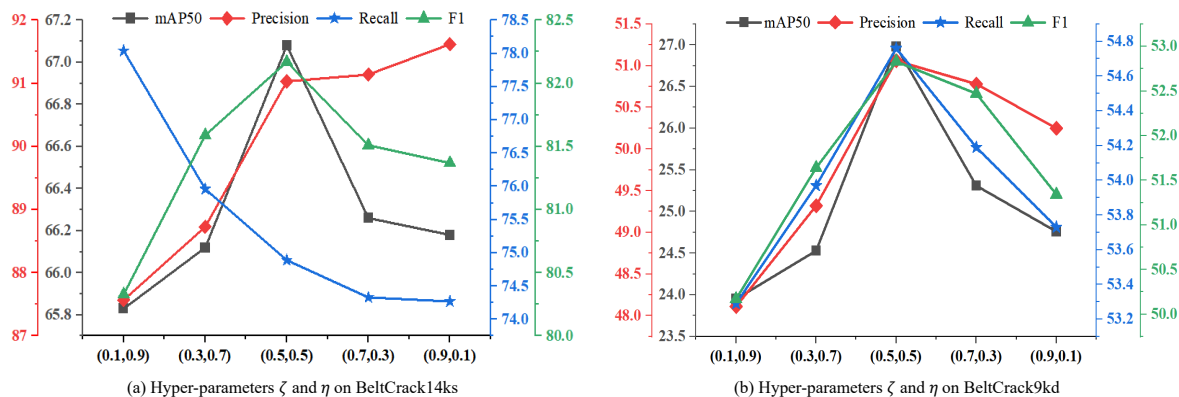


Figure 10: The effects of hyper-parameters ζ and η on our baseline method.

The other is that both \mathcal{L}_{nwd} and \mathcal{L}_{iou} are effective in training. For example, trained by the former, our BeltCrackDet could acquire an mAP₅₀ of 65.77% and an F1 of 80.14% on BeltCrack14ks, only 1.31% lower than the best mAP₅₀ 67.08% and 2.03% lower than the best F1 82.17%, respectively. Merely, they are not the optimal loss functions for our baseline.

(3) Hyper-parameter Effects

To assess the impact of two primary hyper-parameters ζ and η in Eq. (17), we conduct two groups of comparison experiments. Their experiment results are shown in Fig. 10.

In experiments, we change ζ and η to different settings with ζ increasing by a step size 0.2 and η decreasing by a step size 0.2 accordingly, while keeping all other parameters unchanged. We observe that the two parameters have significant impacts on the detection performance of our baseline method. For example, only when $\zeta = 0.5$ and $\eta = 0.5$, our baseline could achieve the best performance on both datasets. In addition, any other hyper-parameter pair (ζ, η) will always cause an obvious performance drop to our baseline.

6. Conclusions

To propel the intelligent technology advancement of learning-based belt crack detection methods, this paper releases the first pair of sequential-based datasets for industrial belt crack detection, and then proposes a baseline method with triple-domain feature learning for both datasets. Experiments show that: (i) our new datasets are usable and effective for learning-based belt crack detection methods, and (ii) our baseline method (BeltCrackDet) is obviously superior to other compared methods, often acquiring the SOTA detection performance on both datasets. One primary weakness of our baseline method is high network complexity and low FPS. In the future, for adapting to real-time industrial applications, how to optimize the deep-network structure of our baseline is worthy of further exploration.

References

- [1] Pengpeng Chen, Dongjingdian Liu, and Shouwan Gao. Non-residual unrestricted pruned ultra-faster line detection for edge devices. *Pattern Recognition*, 137:109321, 2023.
- [2] Wei Wang, Chong Yu, Tengyu Zhang, Feiyu Chen, Yufan Liu, Yaqi Liu, and Zongze Wu. Oversized ore segmentation using sam-enhanced u-net with self-supervised pre-training and semi-supervised self-training. *Expert Systems with Applications*, 285:127980, 2025.
- [3] Jiaqi Tang, Hao Lu, Xiaogang Xu, Ruizheng Wu, Sixing Hu, Tong Zhang, Tsz Wa Cheng, Ming Ge, Ying-Cong Chen, and Fugee Tsung. An incremental unified framework for small defect inspection. In *European conference on computer vision*, pages 307–324. Springer, 2024.
- [4] Guodong Sun, Le Cheng, Jinyu Liu, Yuting Peng, Chengming Xu, Yanwei Fu, Bo Wu, and Yang Zhang. Fs-oredet: Feature enhancement and relationship exploration for boosting few-shot object detector of ore images. *Engineering Applications of Artificial Intelligence*, 133:108437, 2024.
- [5] Miguel Angel Bermeo-Ayerbe, Carlos Ocampo-Martinez, and Javier Diaz-Rozo. Non-intrusive condition monitoring based on event detection and functional data clustering. *Engineering Applications of Artificial Intelligence*, 124:106625, 2023.
- [6] Zekai Zhang, Mingle Zhou, Honglin Wan, Min Li, Gang Li, and Delong Han. Idd-net: Industrial defect detection method based on deep-learning. *Engineering Applications of Artificial Intelligence*, 123:106390, 2023.
- [7] Jianming Zhang, Shigen Zhang, Dianwen Li, Jianxin Wang, and Jin Wang. Crack segmentation network via difference convolution-based encoder and hybrid cnn-mamba multi-scale attention. *Pattern Recognition*, 167:111723, 2025.
- [8] Pasquale Antonante, Heath G. Nilsen, and Luca Carlone. Monitoring of perception systems: Deterministic, probabilistic, and learning-based fault detection and identification. *Artificial Intelligence*, 325:103998, 2023.
- [9] Fen Fang, Liyuan Li, Ying Gu, Hongyuan Zhu, and Joo-Hwee Lim. A novel hybrid approach for crack detection. *Pattern Recognition*, 107:107474, 2020.
- [10] Gongxian Wang, Zhongping Rao, Hui Sun, Chao Zhu, and Zhiqi Liu. A belt tearing detection method of yolov4-belt for multi-source interference environment. *Measurement*, 189:110469, 2022.
- [11] Uttam Kumar Dwivedi, Ashutosh Kumar, and Yoshihide Sekimoto. Real-time classification of longitudinal conveyor belt cracks with deep-learning approach. *PLOS ONE*, 18:1–14, 07 2023.
- [12] Zhuangzhuang Chen, Zhuonan Lai, Jie Chen, and Jianqiang Li. Mind marginal non-crack regions: Clustering-inspired representation learning for crack segmentation. In *2024 IEEE/CVF Conference on Computer Vision and Pattern Recognition (CVPR)*, pages 12698–12708, 2024.

- [13] Jiarui Lei, Xiaobo Hu, Yue Wang, and Dong Liu. Pyramidflow: High-resolution defect contrastive localization using pyramid normalizing flow. In *Proceedings of the IEEE/CVF Conference on Computer Vision and Pattern Recognition (CVPR)*, pages 14143–14152, June 2023.
- [14] Mengyang Pu, Yaping Huang, Qingji Guan, and Haibin Ling. Rindnet: Edge detection for discontinuity in reflectance, illumination, normal and depth. In *Proceedings of the IEEE/CVF International Conference on Computer Vision (ICCV)*, pages 6879–6888, October 2021.
- [15] Zongxin Yang, Jiayu Miao, Yunchao Wei, Wenguan Wang, Xiaohan Wang, and Yi Yang. Scalable video object segmentation with identification mechanism. *IEEE Transactions on Pattern Analysis and Machine Intelligence*, 46(9):6247–6262, 2024.
- [16] Huajun Liu, Xiangyu Miao, Christoph Mertz, Chengzhong Xu, and Hui Kong. Crackformer: Transformer network for fine-grained crack detection. In *Proceedings of the IEEE/CVF International Conference on Computer Vision (ICCV)*, pages 3783–3792, October 2021.
- [17] Xiangkun Hu, Hua Li, Yixiong Feng, Songrong Qian, Jian Li, and Shaobo Li. Ccdformer: A dual-backbone complex crack detection network with transformer. *Pattern Recognition*, 161:111251, 2025.
- [18] Zhuangzhuang Chen, Jin Zhang, Zhuonan Lai, Jie Chen, Zun Liu, and Jianqiang Li. Geometry-aware guided loss for deep crack recognition. In *Proceedings of the IEEE/CVF Conference on Computer Vision and Pattern Recognition (CVPR)*, pages 4703–4712, June 2022.
- [19] Joonmyung Choi, Sanghyeok Lee, Jaewon Chu, Minhyuk Choi, and Hyunwoo J. Kim. vid-ldr: Training free token merging for lightweight video transformer. In *Conference on Computer Vision and Pattern Recognition*, pages 18771–18781, June 2024.
- [20] Hongyang Li, Hao Zhang, Shilong Liu, Zhaoyang Zeng, Tianhe Ren, Feng Li, and Lei Zhang. TAPTR: Tracking Any Point with Transformers as Detection. In *European Conference on Computer Vision*, pages 57–75. Springer, 2024.
- [21] Weiwei Duan, Luping Ji, Shengjia Chen, Sicheng Zhu, and Mao Ye. Triple-domain feature learning with frequency-aware memory enhancement for moving infrared small target detection. *IEEE Transactions on Geoscience and Remote Sensing*, 62:1–14, 2024.
- [22] Linwei Chen, Lin Gu, Dezhi Zheng, and Ying Fu. Frequency-adaptive dilated convolution for semantic segmentation. In *Proceedings of the IEEE/CVF Conference on Computer Vision and Pattern Recognition*, pages 3414–3425, 2024.
- [23] Hehao Zhang, Zhengping Hu, Shuai Bi, Jirui Di, and Zhe Sun. Hmsft: Hierarchical multi-scale spatial-frequency-temporal collaborative transformer for 3d human pose estimation. *Pattern Recognition*, 164:111562, 2025.
- [24] Fan Yang, Lei Zhang, Sijia Yu, Danil Prokhorov, Xue Mei, and Haibin Ling. Feature pyramid and hierarchical boosting network for pavement crack detection. *IEEE Transactions on Intelligent Transportation Systems*, 21(4):1525–1535, 2020.
- [25] Iason Katsamenis, Eftychios Protopapadakis, Nikolaos Bakalos, Andreas Varvarigos, Anastasios Doulamis, Nikolaos Doulamis, and Athanasios Voulodimos. A few-shot attention recurrent residual u-net for crack segmentation. In *Advances in Visual Computing*, pages 199–209, 2023.
- [26] Shreyas Kulkarni, Shreyas Singh, Dhananjay Balakrishnan, Siddharth Sharma, Saipraneeth Devunuri, and Sai Chowdeswara Rao Korlapati. Crackseg9k: A collection and benchmark for crack segmentation datasets and frameworks. In *Computer Vision – ECCV 2022 Workshops*, pages 179–195, Cham, 2023. Springer Nature Switzerland.
- [27] Christian Benz and Volker Rodehorst. Omni-crack30k: A benchmark for crack segmentation and the reasonable effectiveness of transfer learning. In *2024 IEEE/CVF Conference on Computer Vision and Pattern Recognition Workshops (CVPRW)*, pages 3876–3886, 2024.
- [28] Hui Liu, Chen Jia, Fan Shi, Xu Cheng, Mianzhao Wang, and Shengyong Chen. Staircase cascaded fusion of lightweight local pattern recognition and long-range dependencies for structural crack segmentation, 2025.
- [29] Zheng Ge, Songtao Liu, Feng Wang, Zeming Li, and Jian Sun. Yolox: Exceeding yolo series in 2021. *ArXiv*, abs/2107.08430, 2021.
- [30] Mingfei Cheng, Kaili Zhao, Xuhong Guo, Yajing Xu, and Jun Guo. Joint topology-preserving and feature-refinement network for curvilinear structure segmentation. In *2021 IEEE/CVF International Conference on Computer Vision (ICCV)*, pages 7127–7136, 2021.
- [31] Anindya Sundar Das, Guansong Pang, and Monowar Bhuyan. Adaptive deviation learning for visual anomaly detection with data contamination. In *Proceedings of the Winter Conference on Applications of Computer Vision (WACV)*, pages 8845–8854, February 2025.
- [32] Zhengfei Kuang, Tianyuan Zhang, Kai Zhang, Hao Tan, Sai Bi, Yiwei Hu, Zexiang Xu, Milos Hasan, Gordon Wetzstein, and Fujun Luan. Buffer anytime: Zero-shot video depth and normal from image priors. In *Proceedings of the Computer Vision and Pattern Recognition Conference (CVPR)*, pages 17660–17670, June 2025.
- [33] Shahaf E. Finder, Roy Amoyal, Eran Treister, and Oren Freifeld. Wavelet convolutions for large receptive fields. In *Computer Vision – ECCV 2024: 18th European Conference, Milan, Italy, September 29–October 4, 2024, Proceedings, Part LIV*, page 363–380, 2024.
- [34] Feng Yan, Xiaoheng Jiang, Yang Lu, Jiale Cao, Dong Chen, and Mingliang Xu. Wavelet and prototype augmented query-based transformer for pixel-level surface defect detection. In *Proceedings of the Computer Vision and Pattern Recognition Conference (CVPR)*, pages 23860–23869, June 2025.
- [35] Fanbin Lu, Xufeng Yao, Chi-Wing Fu, and Jiaya Jia. Removing anomalies as noises for industrial defect localization. In *Proceedings of the IEEE/CVF International Conference on Computer Vision (ICCV)*, pages 16166–16175, October 2023.
- [36] Tsung-Yi Lin, Priya Goyal, Ross Girshick, Kaiming He, and Piotr Dollár. Focal loss for dense object detection. *IEEE Transactions on Pattern Analysis and Machine Intelligence*, 42(2):318–327, 2020.
- [37] Zhen Yao, Jiawei Xu, Shuhang Hou, and Mooi Choo Chuah. Cracknex: a few-shot low-light crack segmentation model based on retinex theory for uav inspections. In *2024 IEEE International Conference on Robotics and Automation (ICRA)*, pages 11155–11162. IEEE, 2024.
- [38] Ahref Jaziri, Martin Mundt, Andres Fernandez, and Visvanathan Ramesh. Designing a hybrid neural system to learn real-world crack segmentation from fractal-based simulation. In *Proceedings of the IEEE/CVF Winter Conference on Applications of Computer Vision*, pages 8636–8646, 2024.
- [39] Wenxin Ma, Qingsong Yao, Xiang Zhang, Zhelong Huang, Zihang Jiang, and S. Kevin Zhou. Towards accurate unified anomaly segmentation. In *Proceedings of the Winter Conference on Applications of Computer Vision (WACV)*, pages 1342–1352, February 2025.